Extreme Mechanics Letters 4 (2015) 26–37

Contents lists available at ScienceDirect

Extreme Mechanics Letters

journal homepage: www.elsevier.com/locate/eml

Tension-induced tunable corrugation in two-phase soft composites: Mechanisms and implications

Qianli Chen *, Ahmed Elbanna

Department of Civil and Environmental Engineering, University of Illinois at Urbana Champaign, United States

ARTICLE INFO

Article history:
Received 22 May 2015
Received in revised form 23 July 2015
Accepted 27 July 2015
Available online 31 July 2015

Keywords:
Soft composites
Tunable channels
Bio-inspired

ABSTRACT

We numerically investigate the elastic deformation response of a two-phase soft composite under externally applied concentric tension. We show that by carefully designing the inclusion pattern, it is possible to induce corrugations normal to the direction of stretch. By stacking 1D composite fibers to form 2D membranes, these corrugations collectively lead to the formation of membrane channels with shapes and sizes tunable by the level of stretch. Furthermore, we show that by using specific inclusion patterns in laminated plates, it is possible to create pop-ups and troughs enabling the development of complex 3D geometries from planar construction. We have found that the corrugation amplitude increases with the stiffness of inclusion and its eccentricity from the tension axis. We discuss the mechanisms leading to the development of corrugations as well as their different implications. We hypothesize that the techniques discussed in this paper provide greater flexibility and controllability in pattern design and have potential applications in a variety of fields including tunable band gap formation and water treatment.

1. Introduction

Composite materials are ubiquitous in nature [1–4] as well as in industrial applications [5–7]. The combination of the soft and stiff phases usually leads to simultaneous optimization of several mechanical properties including stiffness, toughness and strength [8]. New multifunctional materials are also composite structures. These materials optimize objectives that go beyond mechanical functions to functions such as electrical and thermal conductivities [9], optical properties [2,6] and energy efficiency [10,6]. More recently, the area of programmable metamaterials [5,11] is emerging as a cutting edge research frontier with promising applications in several fields. Many metamaterials may be regarded as a composite material in which the softer phase is voids with different shapes [12,11]. In this paper we focus primarily on polymer reinforced composites in which a soft matrix is reinforced with stiffer inclusions. We investigate the influence of the stiffer phase distribution on the global deformation patterns and its different implications.

Reinforced composites are frequently found as building blocks in tough biological structures [3,13,4,14]. An example usually cited is human bone. Bone is a hierarchical composite of collagen and hydroxyl-apatite with remarkable combination of stiffness and toughness [1,4,7]. The basic building block of bone at the micro scale is mineralized collagen fibrils (MCF) [15] in which the soft collagen matrix is reinforced by platelet inclusions of stiff hydrated calcium phosphates. The mineral plates are elongated in one direction with an in-plane aspect ratio of 8–12 [16]. The common viewpoint is that the apatite plates are not distributed randomly but are rather arranged periodically with a specific staggering pattern [16]. This points to the possible role of pattern design in achieving optimal properties [3]. In this paper, we show that the inclusion pattern controls both in-plane and out-of-plane deformations in the composite and may be used to create complex geometries and designs.

* Corresponding author.
E-mail address: qchen35@illinois.edu (Q. Chen).

http://dx.doi.org/10.1016/j.eml.2015.07.009
2352-4316/

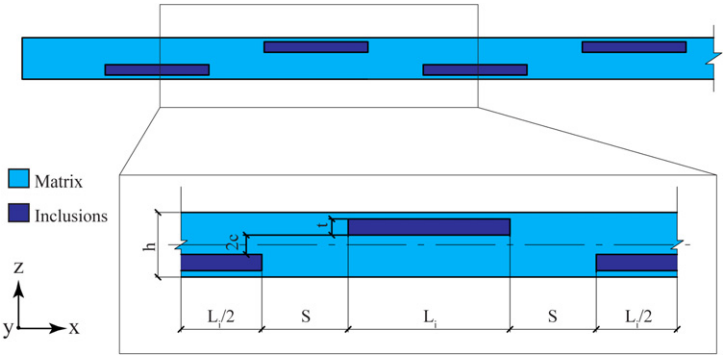

Fig. 1. Geometrical dimensions of unit cell of single composite fibril.

Developing complex and 3D controllable geometries, especially at nano and micro scales, is a topic of immense interests in a variety of fields [17–20]. Significant progress has been made in that field in the last 10 years with the advancement of 3D printing techniques [21] as well as the exploitation of certain mechanical effects such as compressive buckling [20]. Here we show, numerically, that the application of a tensile loading to a reinforced elastomeric fiber with designed inclusion patterns induces local bending deformation modes in the form of corrugations normal to the load application directions. By controlling the distribution of the stiff inclusions within the soft matrix, in a way that is inspired by the staggered patterns of elongated mineral particles in MCF, we are able to control the location, amplitude, and wavelength of these corrugations. This opens new opportunities for hierarchical material design in 2D and 3D.

The remainder of the paper is organized as follows. We describe the model setup and material properties in Section 2. We summarize our results related to tension-induced corrugations in 1D, 2D, and 3D in Section 3. There we examine the different factors affecting the corrugation amplitude such as the elastic moduli ratio of the composite constituents, the aspect ratio of the mineral plates and their location relative to the fibril axis. In Section 4 we discuss our findings, their significance, and potential applications.

2. Material and methods

Geometry: Our starting point is a long and slender polymer fibril (Fig. 1) of total length L and depth h ($L \gg h$). The fibril is reinforced with two rows of staggered platelets with length L_i, width t, offset $c + t/2$ from the fibril axis and inter-platelet spacing $L_i + 2s$. If $s < 0$, the platelets in the two rows are overlapping. A typical unit cell representing the fibril composition is shown in Fig. 1. We choose $L = 1000\ \mu\text{m}$, $h = 30\ \mu\text{m}$ and $t = 7.5\ \mu\text{m}$ for manufacturing convenience but specific values are irrelevant since elasticity equations are scale free. We vary the remaining parameters in a controlled way to explore the design space. We choose micrometer (μm) as a unit of length, and Giga Pascal (GPa) as a unit of stress.

We construct 2D membranes and 3D plates using the composite fibril as a template. Two examples are shown in Fig. 2. The 2D membrane is constructed by gluing the fibrils along their longer edges using a weak polymeric adhesive. The 3D composite plate is constructed by extruding the fibril in the y-direction (normal to the plane of 2D model in Fig. 2(a)). The inclusions are represented by square plates of thickness t.

Material properties: The polymer matrix is modeled as a hyperelastic material using Neo-Hookean constitutive description. We consider two systems: (1) A mixture of two polymers with different elastic moduli, and (2) mineralized polymer matrix. In the first case, the initial Young's modulus of the background polymer matrix is $E_m = 0.005$ GPa corresponding to a commercial rubber [12]. In the second case, the initial Young's modulus for the polymer matrix is $E_m = 1$ GPa which is similar to the value observed for collagen fibers in bone [22]. In both cases the initial Poisson's ratio for the background matrix is $\nu_m = 0.495$ to approximate incompressibility and density of bulk materials is assumed to be 1500 kg/m^3. The inclusions are modeled as hyperelastic material in case (1) and linear elastic minerals in case (2). Several values of (initial) Young's modulus E_i are assumed for the inclusion material to investigate the influence of modulus contrast $r = E_i/E_m$ on the deformation pattern. Here, we vary r between 1 and 50. This range corresponds to the range found in natural materials. For example $r \sim 20$ in mineralized collagen fibrils. Poisson's ratio is assumed to be 0.3 for mineral inclusions and 0.495 for initial value of polymeric inclusions. The weak adhesive used to glue the fibrils in the 2D membrane case is modeled using a bi-linear cohesive law with maximum elongation $\delta_f = 6\ \mu$m, peak strength $T_{ult} = 3$ kPa at $\delta_f/2$ and resulting fracture energy $G_c = 9$ mJ/m^2. Interfacial glue materials of this strength and ductility have been observed in some biological materials [23]. We discuss the practical implications of the cohesive interface modeling assumption in Section 4.

Numerical model: We use the finite element software Abaqus [24] to model the composite fibril and discuss the effect of mesh size on corrugation amplitude results in Appendix A. In 2D models (such as in the fibril and the membrane cases), we use 8-node biquadratic elements to model the behavior of composite fibrils and assume that both ends of the fibrils are clamped. One end is stretched at a constant rate along the longitudinal direction to represent displacement controlled loading while the other end

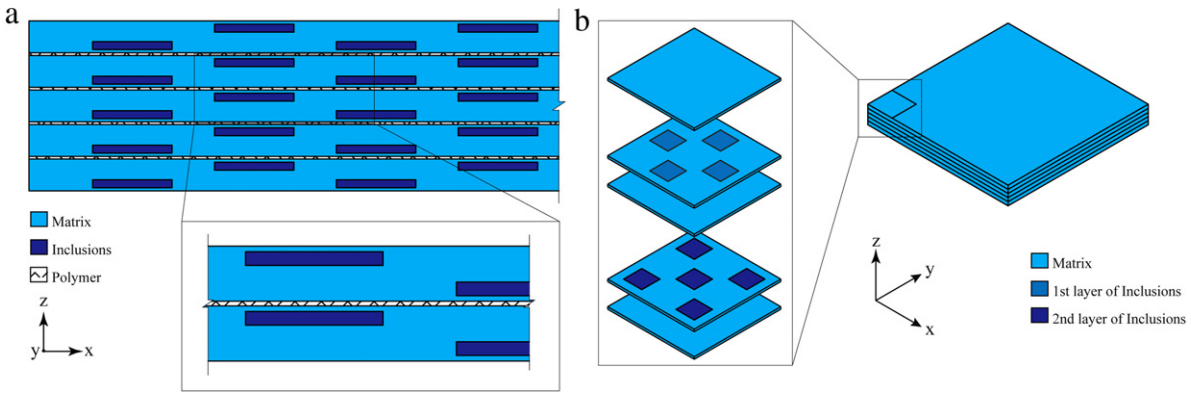

Fig. 2. Geometrical illustration of (a) 2D membranes and (b) 3D plates.

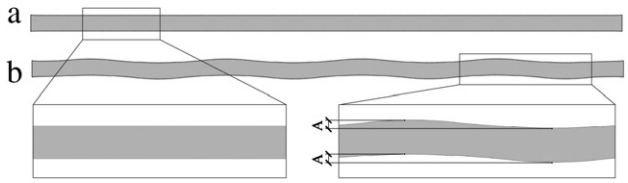

Fig. 3. Deformations of (a) Homogeneous fibril and (b) heterogeneous composite fibril with polymeric inclusions. Corrugations develop in plane stress case of the composite fibril. Results are shown for stretch value of 1.1 (fibril dimensions $L = 1000\ \mu m$, $h = 30\ \mu m$, inclusion dimensions $L_i = 75\ \mu m$, $t = 7.5\ \mu m$ and array distance $c = 4.5\ \mu m$, spacing $s = 40\ \mu m$, polymer–polymer composite with moduli ratio $r = 30$).

is fixed. Both plane stain and plane stress cases are modeled to bound the limits of deformation in finite thickness case. In 3D plate models, we use 8-node linear hex solid elements and clamp two opposite faces for which one face is kept fixed and the other is stretched in the same manner as in the 2D case. In all cases, the stretching rate is small enough to ensure quasi-static loading. However, for a certain range of interfacial strength values in the 2D membrane model, we observed that the quasistatic analysis diverges. For these cases we use a fully dynamic solver with Hilber–Hughes–Taylor time integration to ensure capturing the dynamic instability. Reduced integration is applied to the matrix material and same elements with full integration for the mineral. The displacement field for every load step is computed using the full Newton's method.

3. Results

Tension induced corrugation in the composite fibril:

If a homogeneous elastomeric fibril is stretched, its length increases and width decreases due to the positive Poisson's effect (Fig. 3(a)). However, if the fibril is reinforced with staggered inclusions as shown in Fig. 1(a), it develops a corrugation pattern under stretching. For example, for a modulus ratio $r = 30$ and spacing $s = 40\ \mu m$, the fibril deforms periodically in the direction normal to its axis (Fig. 3(b)). For an elongation of $100\ \mu m$ (i.e. a stretch value of 1.1) in the plane stress case, the amplitude of corrugation is $6.97\ \mu m$ (23% of the fibril depth). The corrugation amplitude A is defined as the difference between peak and valley along one side of composite fibril.

Fig. 4 shows the evolution of corrugation amplitude as a function of stretch for both the plane strain (a) and plane stress (b) cases. Initial deformation is smooth along longitudinal axis (Fig. 4, stretch = 1.02). As stretching continues, the inclusions starts to bend and corrugation amplitude increases rapidly (Fig. 4, stretch = 1.10). In the limit of large stretch (>1.30) most of the deformation concentrates in the matrix material and axial deformations of the elastomer becomes dominant over the bending deformation (Fig. 4 stretch = 1.30). This leads to a reduction in the rate of the growth of the corrugation. The corrugations rate is initially high (up to stretch value ∼1.1). After that, the growth rate decreases and eventually saturates. The plane stress case shows systematically higher corrugation value (for the same value of stretch) and lower Von-Mises stresses than the plane strain case.

The development of corrugation under global tensile loading may be explained using the transformation rule for composites. Static equilibrium for the unit cell shown in Fig. 4 requires that applied tension load at one end is balanced by an equal and opposite collinear load at the other end. Thus the two equilibrating forces are acting along the axis of the fibril. However, due to the presence of inclusions with a different modulus, the center of area of the mineralized section does not coincide with the geometric center. The center of area of a heterogeneous section is computed by transforming the section into an equivalent homogeneous one. This is done by multiplying the area of the stiffer inclusion by the modulus ratio to transform it into an equivalent area of the matrix material. As a results the center of area of the homogenized section is shifted towards the location of the inclusion (see Fig. 4, stretch = 1.10, 1.30). While the loading is uniformly applied at the fibril ends, the shifting in the center of area in the interior section causes eccentricities that follow the periodic inclusion patterns. Accordingly internal moments develop and periodic bending deformation is triggered. As

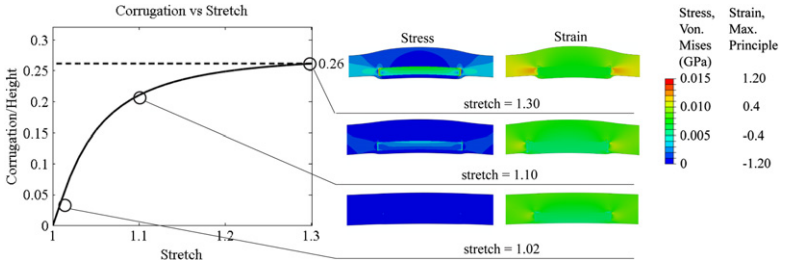

(a) Plane strain.

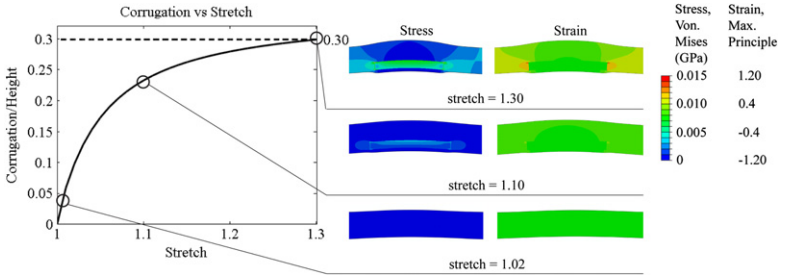

(b) Plane stress.

Fig. 4. Corrugation development as a function of stretch. Successive plots show the deformed shape of the fibril when stretch is 1.02, 1.1 and 1.3 in (a) plane strain and (b) plane stress cases. The corrugation rate increases rapidly in the beginning but then decreases as the deformation becomes stretch dominated (fibril dimension $L = 1000\ \mu$m, $h = 30\ \mu$m, inclusion dimension $L_i = 75\ \mu$m, $t = 7.5\ \mu$m and array distance $c = 4.5\ \mu$m, spacing $s = 40\ \mu$m, moduli ratio $r = 30$).

the corrugation amplitude increases, the center of area of the equivalent homogeneous section is pushed towards the fibril axis and the eccentricity is gradually reduced. This also explains the decrease in the rate of growth of corrugation with increasing stretch (Fig. 4). Throughout the stretch process, the stress level of matrix field is below the ultimate strength of rubber at 0.015 GPa. There is stress concentration at the inclusion corner, but this may be reduced as discussed in Section 4 (see Appendix B).

Effect of inclusion spacing and contrast in elastic moduli:

To investigate the effect of material contrast we consider different values of moduli ratio r equal to 1, 3, 6, 10, 30 and 50 respectively. In each case, we examine the influence of platelet spacing by modeling different values $s = 0, 20, 40, 60, 80\ \mu$m. For generalization, spacing and corrugation are normalized by fibril height to produce dimensionless values. Contours for maximum corrugation at stretch $= 1.3$ are shown as a function of stiffness ratio and normalized spacing in Fig. 5(a) and (b). On one hand, for a fixed value of s, the corrugation amplitude increases as the modulus ratio r increases but eventually levels off. On the other hand, for a fixed value of r, increasing the spacing has only a weak effect on the corrugation amplitude but it does control the corrugation wavelength (not shown here). These results may be explained as follows.

As the modulus ratio increases, the equivalent area of the inclusion becomes larger leading to a higher eccentricity of the center of area and accordingly larger bending deformation. However, if the inclusion modulus is high enough, the inclusion becomes harder to bend. In this case the fibril accommodates the external loading through the stretching of the elastomeric matrix rather than increasing the bending amplitude. The larger the spacing between the inclusions, the larger the volume of the soft matrix that is capable of stretching freely and thus the corrugation amplitude saturates at a lower value of r than in the case of smaller spacing.

The weak dependence of corrugation amplitude on the inclusion spacing at a fixed value of moduli ratio is due to the fact that the spacing does not contribute to the eccentricity of the center of area of the transformed section, the primary source of bending deformation. However, the soft matrix between the inclusions must rotate and elongate to ensure the continuity of the deformed curve of the corrugated beam. Since stretching dominates over bending in the background polymer matrix, the slight rotation contributes to only a slight increase in the deflection in the reinforced portions of the fiber.

Effect of inclusion eccentricity and inclusion aspect ratio:

To investigate the effect of eccentricity and inclusion aspect ratio, we examine different values of c and L_i/t on polymer–polymer composite model. We choose $2c = 3, 6, 9\ \mu$m and vary the aspect ratio between 2 and 12. The results are summarized in Fig. 6.

Lower aspect ratio generates smaller corrugation while increasing the inclusion eccentricity leads to larger corrugation. These observations may be explained as follows. For a fixed inclusion thickness t, the lower the aspect ratio corresponds to shorter length and hence higher inclusion stiffness. As a result, the bending resistance of the inclusion increases, and the wavelength of the corrugation decreases. The deformation is primarily accommodated by elongation in the elastomeric matrix. On the other hand, if the inclusion eccentricity increases, the center of area

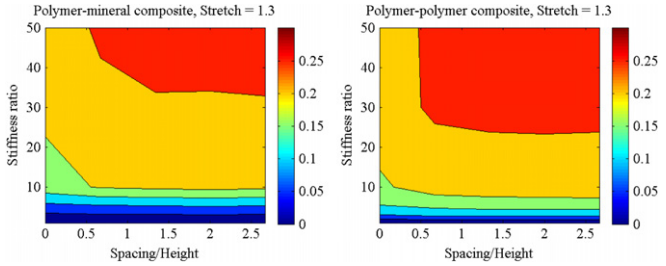

(a) Plane strain.

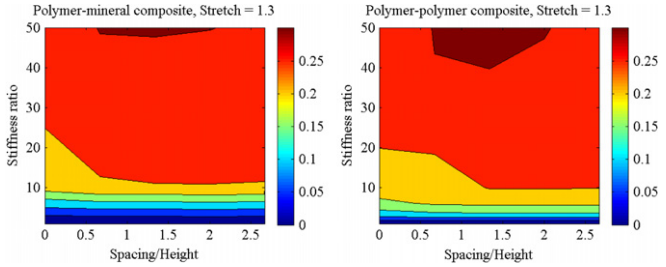

(b) Plane stress.

Fig. 5. Effect of elastic moduli ratio and inclusion spacing on normalized corrugation amplitude (corrugation/height): polymer–polymer model of matrix material with initial Young's modulus $E_m = 0.005$ GPa, inclusion material modeled as hyperelastic material; polymer–mineral model of matrix material with initial Young's modulus $E_m = 1$ GPa, inclusion material modeled as elastic material. The results are presented for both (a) plane strain and (b) plane stress cases (composite fibril dimension $L = 1000\ \mu$m, $h = 30\ \mu$m, $L_i = 75\ \mu$m, $t = 7.5\ \mu$m and array distance $c = 4.5\ \mu$m).

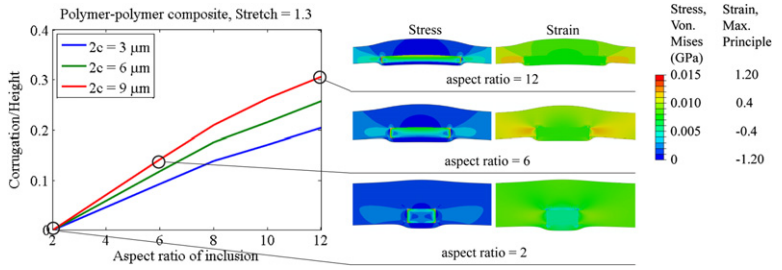

(a) Plane strain.

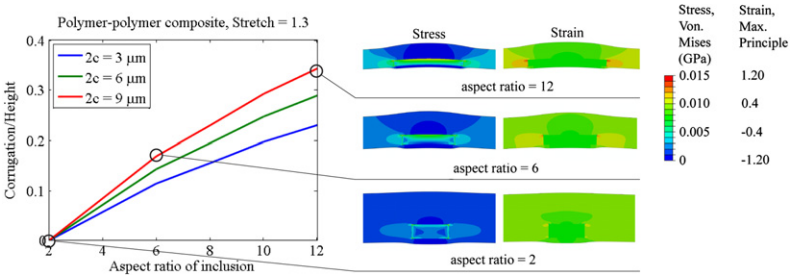

(b) Plane stress.

Fig. 6. Effect of inclusion aspect ratio and eccentricity on normalized corrugation amplitude (corrugation/height) of polymer–polymer model in (a) plane strain and (b) plane stress cases (results are shown corresponding to final stretch = 1.3, fibril dimension $L = 1000\ \mu$m, $h = 30\ \mu$m, inclusion dimension $t = 7.5\ \mu$m, spacing $s = 40\ \mu$m, moduli ratio $r = 100$).

of the transformed section is pushed further away from the fibril axis. As a result the internal bending moment increases and so does the corrugation amplitude.

2D membranes:

Corrugation patterns observed above may be extended to higher dimensions. As a starting point, we consider two composite fibrils that are glued along their longer edge using a weak adhesive described in Section 2. (We discuss briefly the influence of adhesive strength in Appendix C.) The use of an adhesive material along the interface may be necessary for initial assembly of the fibrils and the integrity of the manufacturing process. Also, the adhesive

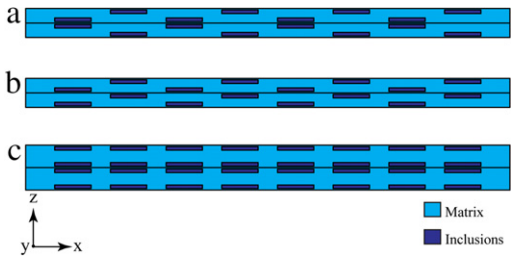

Fig. 7. (a) Symmetric, (b) identical and (c) non-staggered distribution of inclusions.

helps in sealing the inter-fibril openings at the early stages of loading that will otherwise open right away due to fibril contraction in the transverse direction (due to positive Poisson's effect). Three cases with different inclusion distributions are investigated below and are shown schematically in Fig. 7. We show our results for both the plane stress and plane strain cases in Fig. 8.

In the first case, the distribution of inclusions in the two composite fibrils is symmetric about the glue line (Fig. 7(a)). Upon stretching each fibril tends to deform as discussed previously in Section 2. Several contact regions develop. In between these regions, the fibril moves away from one another. If the adhesive is weak enough it will resist the fibril separation for a brief period δ_f and then break leading to the formation of channels as shown in Fig. 8.

The existence of the adhesive ensures that the contact regions remain closed. For a stretch of 1.1 the maximum opening at the channel location is 12.87 μm in plane strain case and 13.88 μm in plane stress. Recalling that the corrugation amplitude is dependent on the stretch (Fig. 4), and since both the matrix and the inclusions are operating within their elastic regime, we argue that the procedure introduced here may be a viable tool for constructing membranes with tunable channel sizes. We discuss the implications of this in Section 4.

In the second case, the two fibrils have identical distribution of inclusions (Fig. 7(b)). Upon stretching, the two fibrils conform to one another and interlock (Fig. 8). The adhesive strength is adequate to keep the crevices size under maximum elongation δ_f and prevent the fibrils from separation. The oblique orientation of the sealed crevices, however, may be useful in generating certain band gap patterns. This will be explored elsewhere.

In the third case, the two fibrils have identical distribution of aligned inclusions as above (Fig. 7(c)). Within each fibril the inclusions are symmetrically distributed about the fiber axis. Upon stretching, no corrugation will form in either fibril as expected. However, the softer matrix within the spacing between the inclusions contracts laterally more than the stiffened portions (Fig. 9). In plane strain case, since the contraction within the softer regions is larger than the adhesive capacity, the adhesive layer detaches and periodic channels form as shown in Fig. 9(a). In plane stress case, as contraction is smaller, weak adhesive ensures that the openings remains completely sealed (Fig. 9(b)).

We note that in all these cases with weak cohesive strength, the channels develop gradually in response to the applied loading (see video S1 in supplementary material as well as Appendix C). No instability or transition to dynamic crack growth is observed. A possible explanation is that due to the corrugation patterns of the joined fibrils, there is always a closed contact region ahead of the crack tip (corresponds to fibrils moving towards one another). This local compression stabilizes the channel growth and opening. However, with stronger cohesive strength and steeper softening slope, the interaction between the fibril elastic stiffness and the interfacial stiffness may lead to dynamic instability and a sudden opening of the channels. This is discussed briefly in Appendix C (see also the supplementary video S2) and is a subject of ongoing investigations.

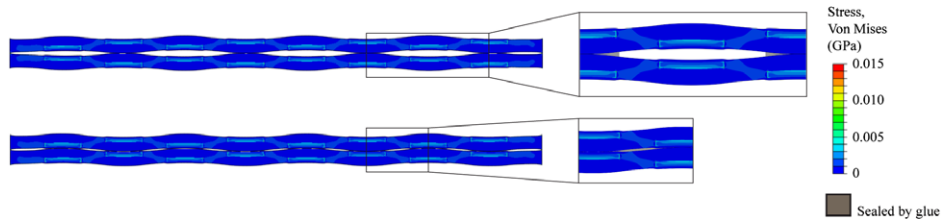

(a) Plane strain.

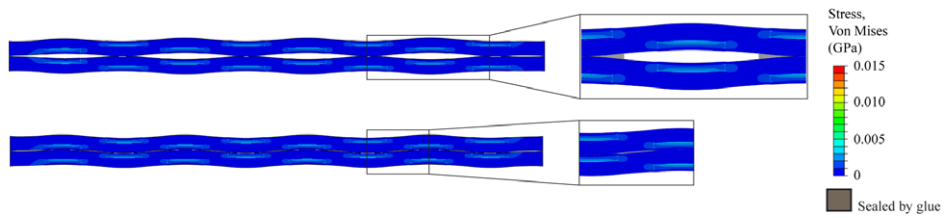

(b) Plane stress.

Fig. 8. Deformation of two composite fibrils with symmetric and identical staggered distribution of inclusions in (a) plane strain and (b) plane stress cases: (1.1 Stretch on polymer–polymer materials with matrix initial Young's modulus $E_m = 0.005$ GPa, inclusion material modeled as hyperelastic material, composite fibril dimension $L = 1000$ μm, $h = 30$ μm, inclusion dimension $L_i = 75$ μm, $t = 7.5$ μm, spacing $s = 40$ μm, moduli ratio $r = 30$).

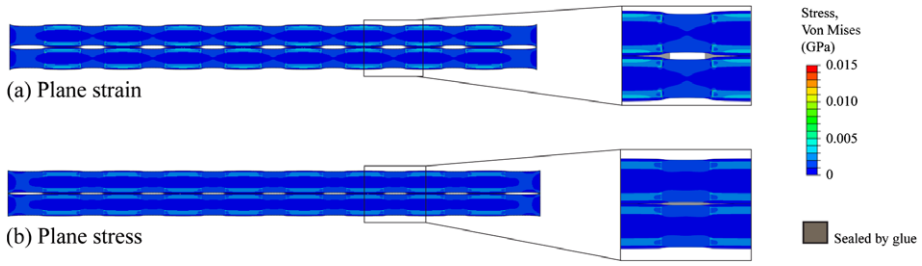

Fig. 9. Deformation of two composite fibrils with non-staggered distribution of inclusions in (a) plane strain and (b) plane stress cases: (array distance $c = 12\ \mu$m, other parameter same as Fig. 8).

3D plates

Tension induced corrugation may be used in designing controllable non-planar geometries from planar sheets of material. Recall from Fig. 2 that the 3D construction is essentially a laminated plate in which the reinforcing inclusions exist in the second and fourth layers. Here we consider the case of a mineralized polymer composite with material properties similar to the collagen hydroxyapatite composite. The generated corrugation pattern depends critically on the distribution of the stiff inclusions in-plane and through the thickness direction. Three cases are investigated and are shown in Fig. 10 as proof-of-concept. In the first case (Fig. 10(a)), the inclusions are staggered sheets placed with their longitudinal axis normal to the loading direction. This geometry is developed by extruding composite fibril in the y-direction (see Fig. 1) and the corrugation pattern is alternating valleys and crest regions parallel to the y-axis. In the second case (Fig. 10(b)), the inclusions are square plates staggered in the thickness direction but are aligned along the x-direction. The corrugation pattern resembles a regular egg-box. In the third case (Fig. 10(c)), the inclusions are staggered in plane and through thickness. The resulting corrugation pattern is similar to a skewed egg-box. This technique may be further used to develop surfaces of tunable roughness profile that depends on the level of deformation by carefully designing the inclusion pattern. Guttag and Boyce [25] have recently used a similar idea to develop surfaces that get rougher by the application of compressive loading on a reinforced composite.

4. Discussion and conclusions

In this paper we present a numerical model for the deformation of a two-phase elastic composite under uniaxial stretch and explore some of its possible design implications. One phase is chosen to be a polymer while the inclusion phase may be either a mineral or another polymer. Such composites are abundant in natural materials such as bone [1,4,7] and sea sponge [2] as well as in engineered materials such as fiber reinforced concrete [26], asphalt concrete [27] and nanofiller reinforced rubber [28]. Extensive studies have been carried out, using homogenization theory, to characterize the effective properties of these composites at the macroscale based on their microstructure [29–31]. A point of departure in the current investigation is the use of inclusions of comparable dimensions to the overall composite dimensions and thus the whole composite is analyzed and not just a representative unit cell. This opens new opportunities for identifying unexpected deformation patterns that may be suppressed in the homogenized representation.

Inclusions in polymeric matrix have been previously used to control the mechanical [32,18,25], thermal [9], and toughness properties of the resulting composite as well as to add functionality [6]. An essential contribution of the current work is pointing to the additional role of inclusions in controlling the deformation pattern of the composite globally. In particular, we show that under externally concentric tensile loading, the internal distribution of the inclusions may lead to local bending modes and development of periodic corrugation patterns. These corrugations are exploited to construct complex 2D and 3D geometries.

The development of corrugation in a single composite fibril may be explained on the basis of the transformation theory of composites. While the external load is concentric, the inclusions change the effective stiffness along the fibril length leading to the development of internal eccentricities and thus bending deformation. The resulting corrugations increase with the inclusion stiffness and eccentricity from the fibril axis. The corrugation amplitude also weakly depends on the inclusion spacing.

While corrugations in a single fibril may be of little interest in its own, the potential for exploiting this phenomenon in 2D and 3D may lead to several interesting applications. For example, we show that by assembling composite fibers with different inclusion distributions in the plane, the stretch-induced corrugation in each individual fibril may collectively lead to the formation of channels of different shapes and orientation within the composite sheet. The size of these channels is a function of the applied stretch and hence is tunable. The elasticity of the constituent materials ensures that the deformations, including the opening of the channels, is reversible and hence may be reproduced repeatedly. In this particular case, effect of fatigue response must be considered. This is beyond the scope of the current paper.

In this paper, the interfacial glue used in constructing 2D membranes from 1D fibrils is modeled using cohesive elements. This modeling assumption may be justified by the confinement of separation between the fibrils to the well-defined interfacial region and the small thickness of the glue layer relative to the dimensions of the joined fibrils. In case of thicker interfaces, or if distributed damage is expected to occur outside the interfacial region, or

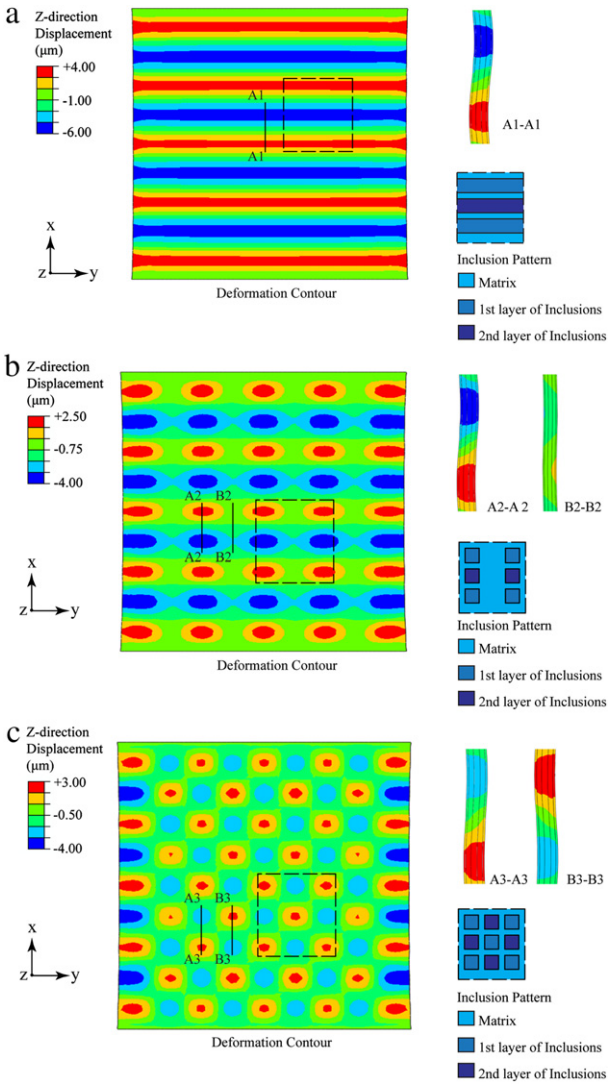

Fig. 10. Inclusion distribution and corrugation patterns in a composite plane: (a) inclusion platelet size = 1000 μm×75 μm×7.5 μm, spacing = 32.5 μm, maximum corrugation = 8.2 μm at surface; (b) inclusion size = 75 μm × 75 μm × 7.5 μm, 32.5 μm spacing along stretch direction, 140 μm spacing perpendicular to stretch direction. Maximum corrugation = 5.4 μm at surface; (c) inclusion size = 75 μm × 75 μm × 7.5 μm, 32.5 μm spacing in both directions, maximum corrugation = 4.9 μm at surface. (Results are shown for stretch = 1.1, plate size = 1000 μm × 1000 μm × 30 μm, matrix material with initial Young's modulus $E_m = 5$ GPa, $\nu_m = 0.495$, inclusion material modeled as elastic material, $E_i = 100$ GPa, $\nu_i = 0.28$).

if diffusion effects are important, a more refined model may be required. For example, the glue may be modeled explicitly with bulk elements or a continuum damage model may be used. Moreover, our simulations suggest that the fibrils remain within their elastic limits even after interfacial separation and channel opening. This suggests that their deformation may be reversed upon reducing the stretch and the channels may be closed if desired. The closure of the channels may provide an opportunity for the self-healing of the glue layer if its chemistry allows. An example of such self-healing interfaces may be polymers with hindered urea bonds [33]. This facilitates the reversibility of the process.

It was previously shown that it is possible to change the void patterns in an elastomer through compressive buckling leading to tunable band gaps and auxetic response [34]. The current approach may provide additional flexibility and more controllability over this process. In particular the void shapes and sizes in the current case are tuned by the amplitude of stretch. Tension-like loading is more easily controlled than instabilities induced by buckling. Moreover, tension loading will not induce undesired out of plane instabilities that may sometimes occur under compressive loading. The voids are not introduced a priori in the elastomer but they develop and are patterned following the inclusion distribution. This may be a more flexible way, from a manufacturing perspective, to generate holes in the polymer matrix, than to precisely machine these holes from the beginning.

Developing complex 3D geometries, especially at nano and micro scale, is a topic of immense interests in a variety of fields [17–20]. The recent advances in 3D printing [21] as well as in origami engineering [35,36] have opened new

opportunities in that realm that were not thought of a few years back. Here we show that by designing the distribution of inclusions in a polymer laminated plate, it is possible to create pop-ups and valleys in the plate with controllable pattern. While the amplitude of corrugations is about 25% of the plate thickness, we hypothesize that it may play a role in increasing the plate toughness by adding geometric non-planarity in the crack path. This mechanism has been identified previously in several systems including graphene sheets [37] and rough faults [38]. We conjecture that this inclusion-patterned non-planarity may be playing a role in the toughness of biological composites such as mineralized collagen fibril. This is a topic of further investigation.

While the system investigated in this paper has several exciting features and potential applications, it does suffer from a number of limitations. For example, we have observed that the corrugation saturates beyond a certain value of stretch. Currently we are able to achieve maximum corrugation amplitude 25%–30% of the fibril thickness. Moreover, due to the elasticity of the system the deformations are recovered upon removal of loads. While this may be a desirable property, it points to the fact that the loads have to be kept on the system during its operation in order to maintain the desired corrugation amplitude or channel geometry. While we do not see this as a problem in the envisioned applications, we acknowledge that this may be a limitation compared to other systems in which complex geometries are produced by plastic deformation or inelastic buckling. Finally, we have observed some stress concentration at the matrix-inclusion interfaces especially if the inclusion has sharp edges. We ran another simulation (shown in Appendix B) in which we use inclusions with rounded corners. Our preliminary result suggests that, by rounding the inclusion corner the stress concentration is greatly reduced. This preliminary investigation suggests that the problem of stress concentration is controllable and will not have a detrimental impact on the performance of the system. We also note that the stretch magnitude considered here (<1.3) is relatively small and we do not expect cavitation phenomena to limit the response. Detailed investigation of the interfacial response as well as the potential for cavitation will be reported elsewhere.

A future extension of this study will involve investigation of different potential applications of controllable tension-induced corrugations. For example, the ability to control the void sizes and shapes may be very useful in fluid treatment applications and may be advantageous over filters with constant mesh size. Moreover, by changing the voids topology it is possible to develop tunable band gaps. Furthermore, the effect of tension-induced non-planarity in 3D plates on fracture toughness and surface roughness development warrants further investigation particularly in the context of biological composites.

Appendix A. Mesh sensitivity analysis

We conduct a numerical experiment to analyze the effect of mesh refinement on the results of corrugation amplitude. The benchmark problem we study is the corrugation of single fibril under stretch in both plane stress and plane strain cases. The material and geometry properties are same as shown in Fig. 4. The corrugation amplitudes at 1.10 and 1.30 stretch are illustrated in Fig. A.1.

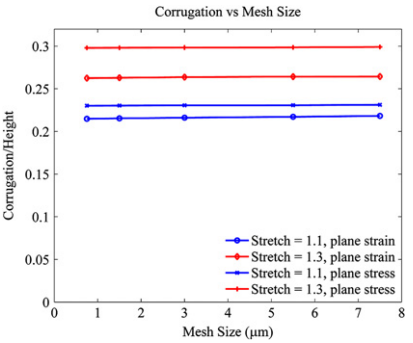

Fig. A.1. Mesh sensitivity effects of single fibril under stretch.

Fig. A.1 shows that the corrugation amplitude converges as mesh size approaches 0 and the results vary in magnitude of 0.01 μm in absolute corrugation amplitude depending on mesh size. In that case, we choose global mesh size to be 1 μm in balance of cost and precision.

Appendix B. Effect of inclusion corners

Stretching the composite fibril causes stress concentration near the edges of inclusions when inclusions have sharp corners (Fig. B.1(a)). The maximum value of hydrostatic stress (average of the three normal stress components) within the matrix material is 0.012 GPa in plane strain case and 0.0024 GPa in plane stress case. The former value may lead to cavitation instabilities. To reduce the stress concentration in the plane strain case, we model a system with rounded inclusion corners (Fig. B.1(b)). The hydrostatic stress of matrix is reduced by more than a factor of 2–0.0047 GPa. Thus, susceptibility to fracture and cavitation may be greatly reduced by tailoring the geometry of the elongated inclusion in our system.

Appendix C. Effect of cohesive interfacial strength

The dynamics of channel opening in 2D membrane is controllable by adjusting the strength of the cohesive interfaces. Here we report on our preliminary investigations on the effect of the cohesive interface properties on the dynamics of channel growth. We conduct a series of models simulating two composite fibrils with different cohesive interfacial strength T_{ult} and stiffness (Fig. C.1(a)). The results show three regions of behavior depending on the peak cohesive strength. For weak strength (Fig. C.1(b), $T_{ult} < 3$ kPa), the deformation remains quasistatic, the channel expands gradually (Fig. C.2(a)) and the interfacial openings develop smoothly (Fig. C.3(a)). For higher cohesive strength values (Fig. C.1(b), $T_{ult} > 30$ kPa), the glue never break completely and it continues to seal the interface with no opening development between the two fibrils. For intermediate values of cohesive strength (Fig. C.1(b), 3 kPa $< T_{ult} <$ 30 kPa), there will be a dynamic instability.

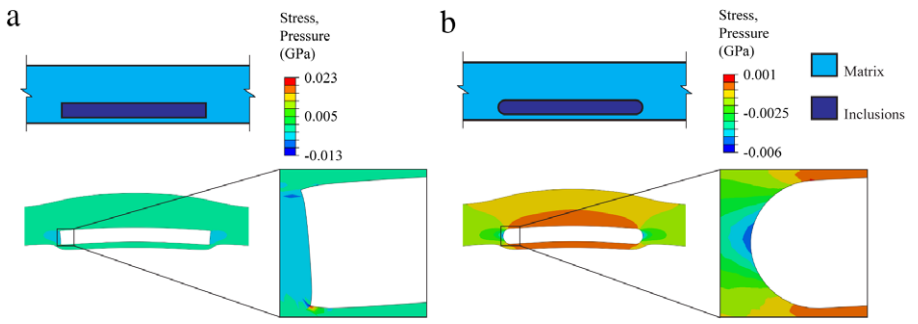

Fig. B.1. Local hydrostatic pressure distribution in matrix near corner of inclusion in plane strain case: (a) Perfect interface with sharp corner; (b) Glued interface modeled by cohesive law; (c) Rounded inclusion with perfect interface.

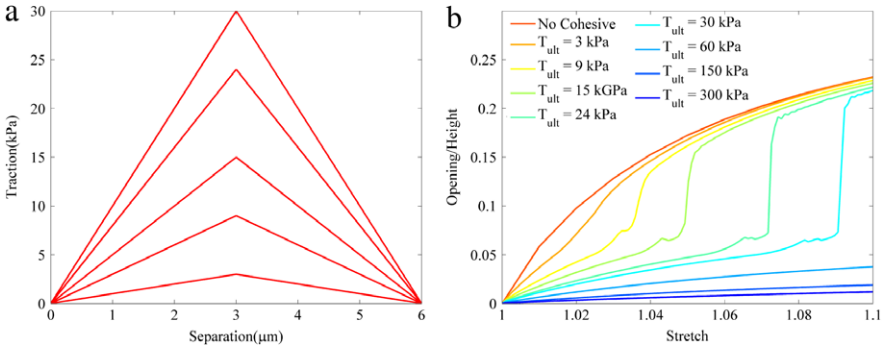

Fig. C.1. (a) Cohesive laws with different cohesive strength T_{ult} at $\delta_f/2$, $\delta_f = 6$ μm; (b) Effect of cohesive strength on corrugation development (polymer–polymer materials with matrix initial Young's modulus $E_m = 0.005$ GPa, inclusion material modeled as hyperelastic material, composite fibril dimension $L = 1115$ μm, $h = 30$ μm, inclusion dimension $L_i = 75$ μm, $t = 7.5$ μm, spacing $s = 40$ μm, moduli ratio $r = 30$).

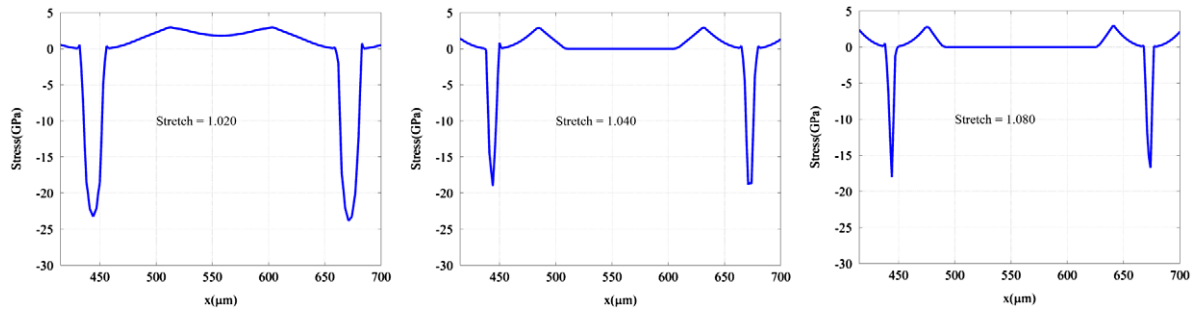

(a) $T_{ult} = 3$ kPa.

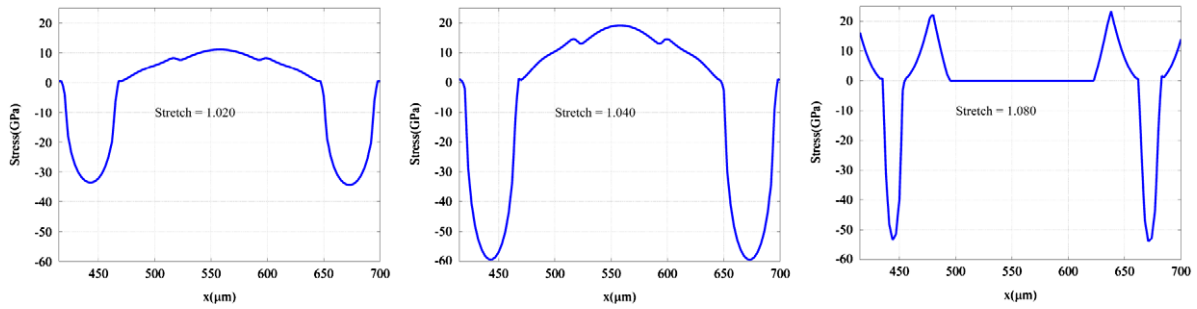

(b) $T_{ult} = 24$ kPa.

Fig. C.2. Cohesive stress (positive for tension and negative for compression) distribution along one opening position: (a) Cohesive strength $T_{ult} = 3$ kPa; (b) Cohesive strength $T_{ult} = 24$ kPa.

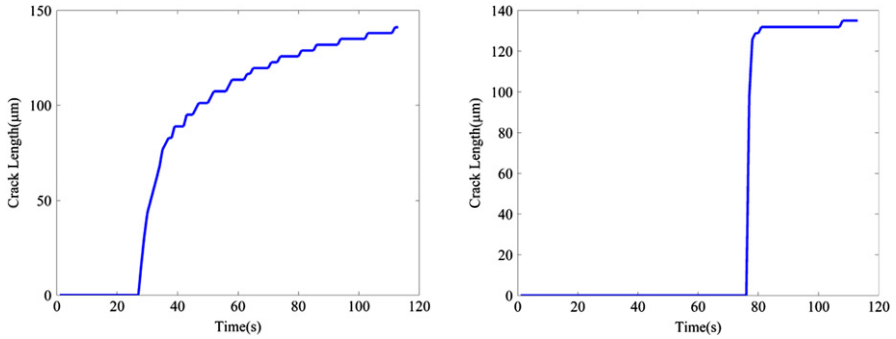

(a) $T_{ult} = 3$ kPa. (b) $T_{ult} = 24$ kPa.

Fig. C.3. Crack length (Opening with detachment of cohesive law): (a) Cohesive strength $T_{ult} = 3$ kPa; (b) Cohesive strength $T_{ult} = 24$ kPa (stretch rate $= 1\ \mu m/s$).

The inter-fibril channels will open abruptly (Fig. C.1(b)), causing sudden loss of the cohesive traction (Fig. C.2(b)) and a jump in the channel growth rate (Fig. C.3(b)). Videos of corrugation development are attached in supplementary materials (S1, $T_{ult} = 3$ kPa; S2, $T_{ult} = 15$ kPa; S3, $T_{ult} = 60$ kPa).

The interaction between the elastic stiffness of the fibrils and the interfacial properties lead to a rich behavior ranging between quasistatic deformation and dynamics instabilities. The interfacial properties may not be only characterized by fracture energy (as in the case of Griffith's interfaces) but additional parameters such as peak cohesive strength and softening slope may play an important role as shown above. In particular a full characterization of the cohesive behavior may be required to investigate the transition from ductile to brittle interfacial response (and correspondingly the switch between stable channel growth and dynamic channel growth). Detailed study of this topic will be a focus of further investigations.

Appendix D. Effect of different glue strength on the dynamics of inter-fibrillar channel growth

Supplementary material related to this article can be found online at http://dx.doi.org/10.1016/j.eml.2015.07.009.

References

[1] S. Weiner, H.D. Wagner, The material bone: Strucutre-mechanical function relations, Annu. Rev. Mater. Sci. 28 (1998) 271–298.
[2] J. Aizenberg, V.C. Sundar, A.D. Yablon, J.C. Weaver, G. Chen, Biological glass fibers: Correlation between optical and structural properties, Proc. Natl. Acad. Sci. USA 101 (10) (2004) 3358–3363.
[3] H.D. Espinosa, J.E. Rim, F. Barthelat, M.J. Buehler, Merger of structure and material in nacre and bone—perspectives on de novo biomimetic materials, Prog. Mater. Sci. 54 (8) (2009) 1059–1100.
[4] J.W.C. Dunlop, P. Fratzl, Biological composites, Annu. Rev. Mater. Res. 40 (1) (2010) 1–24.
[5] N. Engheta, R.W. Ziolkowski, Metamaterials: Physics and Engineering Explorations, 2006.
[6] K.A. Arpin, A. Mihi, H.T. Johnson, A.J. Baca, J.A. Rogers, J.A. Lewis, et al., Multidimensional architectures for functional optical devices, Adv. Mater. 22 (10) (2010) 1084–1101.
[7] U.G.K. Wegst, H. Bai, E. Saiz, A.P. Tomsia, R.O. Ritchie, Bioinspired structural materials, Nature Mater. 14 (1) (2015) 23–36.
[8] X. Guo, H. Gao, Bio-Inspired Material Design and Optimization, 2006.
[9] Y.C. Shin, E. Novin, H. Kim, Electrical and thermal conductivities of carbon fiber composites with high concentrations of carbon nanotubes, Int. J. Precis. Eng. Manuf. 16 (3) (2015) 465–470.
[10] F. Tarlochan, S. Ramesh, Composite sandwich structures with nested inserts for energy absorption application, Compos. Struct. 94 (3) (2012) 904–916.
[11] B. Florijn, C. Coulais, M. Van Hecke, Programmable mechanical metamaterials, Phys. Rev. Lett. 113 (17) (2014).
[12] K. Bertoldi, M.C. Boyce, Wave propagation and instabilities in monolithic and periodically structured elastomeric materials undergoing large deformations, Phys. Rev. B—Condens. Matter Mater. Phys. 78 (18) (2008).
[13] G.M. Luz, J.F. Mano, Mineralized structures in nature: Examples and inspirations for the design of new composite materials and biomaterials, Compos. Sci. Technol. 70 (13) (2010) 1777–1788.
[14] R.O. Ritchie, The conflicts between strength and toughness, Nat. Mater. 10 (11) (2011) 817–822.
[15] I. Jäger, P. Fratzl, Mineralized collagen fibrils: A mechanical model with a staggered arrangement of mineral particles, Biophys. J. 79 (4) (2000) 1737–1746.
[16] P. Fratzl, N. Fratzl-Zelman, K. Klaushofer, G. Vogl, K. Koller, Nucleation and growth of mineral crystals in bone studied by small-angle X-ray scattering, Calcif. Tissue Int. 48 (1991) 407–413.
[17] V.B. Shenoy, D.H. Gracias, Self-folding thin-film materials: From nanopolyhedra to graphene origami, MRS Bull. 37 (9) (2012) 847–854.
[18] A.R. Studart, Biological and bioinspired composites with spatially tunable heterogeneous architectures, Adv. Funct. Mater. 23 (36) (2013) 4423–4436.
[19] J. Lee, C.Y. Koh, J.P. Singer, S. Jeon, M. Maldovan, O. Stein, et al., 25th anniversary article: Ordered polymer structures for the engineering of photons and phonons, Adv. Mater. 26 (4) (2014) 532–569.
[20] S. Xu, Z. Yan, K.-I Jang, W. Huang, H. Fu, J. Kim, et al., Assembly of micro/nanomaterials into complex, three-dimensional architectures by compressive buckling, Science 347 (6218) (2015) 154–159.
[21] S.M. Peltola, F.P.W. Melchels, D.W. Grijpma, M. Kellomäki, A review of rapid prototyping techniques for tissue engineering purposes, Ann. Med. 40 (4) (2008) 268–280.
[22] M.J. Buehler, Molecular nanomechanics of nascent bone: Fibrillar toughening by mineralization, Nanotechnology 18 (29) (2007).
[23] G.E. Fantner, T. Hassenkam, J.H. Kindt, J.C. Weaver, H. Birkedal, L. Pechenik, et al., Sacrificial bonds and hidden length dissipate energy as mineralized fibrils separate during bone fracture, Nature Mater. 4 (8) (2005) 612–616.
[24] Abaqus Analysis User's Manual, 6.13th ed., Dassault Systemes Simulia Corp., Providence, RI, USA, 2013.
[25] M. Guttag, M.C. Boyce, Locally and dynamically controllable surface topography through the use of particle-enhanced soft composites, Adv. Funct. Mater. 25 (24) (2015) 3641–3647.
[26] R.F. Zollo, Fiber-reinforced concrete: An overview after 30 years of development, Cem. Concr. Compos. 19 (2) (1997) 107–122.
[27] S.M. Abtahi, M. Sheikhzadeh, S.M. Hejazi, Fiber-reinforced asphalt-concrete—a review, Constr. Build. Mater. 24 (6) (2010) 871–877.

[28] S. Thomas, R. Stephen, Rubber Nanocomposites: Preparation, Properties, and Applications, 2010.
[29] M. Åberg, P. Gudmundson, The usage of standard finite element codes for computation of dispersion relations in materials with periodic microstructure, J. Acoust. Soc. Am. 102 (4) (1997) 2007–2013.
[30] B. Hassani, E. Hinton, A review of homogenization and topology optimization I—homogenization theory for media with periodic structure, Comput. Struct. 69 (6) (1998) 707–717.
[31] H. Sun, S. Di, N. Zhang, C. Wu, Micromechanics of composite materials using multivariable finite element method and homogenization theory, Internat. J. Solids Structures 38 (17) (2001) 3007–3020.
[32] R. Libanori, R.M. Erb, A. Reiser, H. Le Ferrand, M.J. Süess, R. Spolenak, et al., Stretchable heterogeneous composites with extreme mechanical gradients, Nature Commun. 3 (2012).
[33] H. Ying, Y. Zhang, J. Cheng, Dynamic urea bond for the design of reversible and self-healing polymers, Nature Commun. 5 (2014).
[34] J.T.B. Overvelde, K. Bertoldi, Relating pore shape to the non-linear response of periodic elastomeric structures, J. Mech. Phys. Solids 64 (1) (2014) 351–366.
[35] E. Hawkes, B. An, N.M. Benbernou, H. Tanaka, S. Kim, E.D. Demaine, et al., Programmable matter by folding, Proc. Natl. Acad. Sci. USA 107 (28) (2010) 12441–12445.
[36] E.A. Peraza-Hernandez, D.J. Hartl, R.J. Malak Jr., Design and numerical analysis of an SMA mesh-based self-folding sheet, Smart Mater. Struct. 22 (9) (2013).
[37] T. Zhang, X. Li, H. Gao, Designing graphene structures with controlled distributions of topological defects: A case study of toughness enhancement in graphene ruga, Extreme Mech. Lett. 1 (2014) 3–8.
[38] E.M. Dunham, D. Belanger, L. Cong, J.E. Kozdon, Earthquake ruptures with strongly rate-weakening friction and off-fault plasticity, part 2: Nonplanar faults, Bull. Seismol. Soc. Amer. 101 (5) (2011) 2308–2322.